

Computing finite-temperature elastic constants with noise cancellation

Debashish Mukherji,¹ Marcus Müller,¹ and Martin H. Müser²

¹*Institut für Theoretische Physik, Georg-August-Universität Göttingen, 37077 Göttingen, Germany*

²*Dept. of Materials Science and Engineering, Saarland University, 66123 Saarbrücken, Germany*

Elastic constants are central material properties, frequently reported in experimental and theoretical studies. While their computation is straightforward in the absence of thermal fluctuations, finite-temperature methods often suffer from poor signal-to-noise ratios, the presence of strong anharmonic effects, or require second-order derivatives with respect to spatial coordinates to be taken. Here, we show how to compute elastic constants in thermal ordered and disordered systems by generalizing a noise-cancellation method originally developed for piezoelectric coupling coefficients. A slight strain is applied to an equilibrated solid. Simulations of both the strained and unstrained (or oppositely strained) reference systems are performed using identical thermostatting schemes. As demonstrated theoretically and with generic one-dimensional models, this allows stress differences to be evaluated and elastic constants to be determined with favorable thermal noise. We then apply this approach across a diverse set of systems, spanning crystalline argon, ordered silicon as well as amorphous silicon, poly(methyl methacrylate), and cellulose derivatives.

I. INTRODUCTION

Elastic constants are routinely computed in molecular simulations using two mainstream methods: response-to-deformation (RTD) [1] and fluctuation-based (FB) [2, 3] computations. Their central ideas are as follows: When deforming a solid from a stress-free state, the strain tensor elements, ε_i in Voigt notation, are known, and the resulting stress-tensor elements, σ_i , can be computed. The elastic tensor elements, C_{ij} , then follow from $\sigma_i = C_{ij}\varepsilon_j$. Alternatively, the simulation box can be fixed, and an estimator be evaluated, which consists of a so-called Born term and a stress-fluctuation correction [4, 5]. The Born term hinges on the Hessian matrix and is thus frequently not available, in particular for many-body or machine-learned potentials. Analyzing box-shape fluctuations in constant-stress simulations is also a viable approach [2] provided that meaningful barostats are employed, which can be difficult to find in standard software. Worth mentioning is also the determination of elastic constants through the computation of the sound velocity [6, 7], which can be regarded as a FB method. This approach, however, relies on analyzing dynamical rather than static covariances.

Each of the mainstream methods includes further sub-methods [8, 9]. For example, at zero temperature it suffices to compute the energy as a function of strain, although internal modes must be allowed to relax in a non-affine fashion if applicable [1, 9]. Alternatively, one can compute second-order derivatives of the energy with respect to atomic coordinates, where non-affine displacements can again cause complications [1, 9], in particular for a stressed reference [10]. Additional modifications apply in the presence of thermal fluctuations [4, 5, 11] or, again, when the reference is stressed [10]. Accounting for quantum fluctuations, not considered here, requires additional terms [12, 13].

RTD and FB computations of elastic tensor elements each have their own advantages and disadvantages.

In particular, FB computations require long convergence times; using larger system sizes even increases the stochastic error, given fixed compute time, while the RTD method would leave it constant. However, RTD computations using simple forward-difference schemes and conducted at what may deceptively be considered a small strain, say, 1%, can produce errors in the elastic constants on the order of 10% due to nonlinear effects, whereas simulations at smaller strains are dominated by stochastic noise.

An alternative to the above-mentioned algorithms is based on the diagonalization of the Hessian matrix while accounting for non-affine deformations in the system. Although such approaches are computationally expensive, particularly for large system sizes, they yield exact results in the absence of thermal fluctuations and allow local elastic constants to be defined [14, 15]. When the temperature is finite, anharmonic effects set in, which can be captured by considering the Hessian of the instantaneous rather than the relaxed normal modes [16]. However, the occurrence of negative eigenvalues in the Hessian makes a rigorous error estimate difficult. Even the computation of viscoelastic properties of ultra-strong disordered systems, which lack barrier crossings, is complex when done with care [17]. In this context, the present work focuses on a lean computation of only the elastic tensor, prioritizing minimal implementation, low noise, and minimal systematic errors.

Here, we extend a noise-cancellation technique originally developed for the piezoelectric coefficient γ of α -quartz, which remained effective even near the α - β quartz transition temperature [18]. The method contrasted the strain in two constant-stress simulations, both initialized from the same equilibrated configuration and both using the same random number sequence in the thermostat. In one sample, an electric field was applied, which slowly increased over time, while the other sample remained field-free. The strain difference between the samples was essentially free of thermal fluctuations—at least during the initial stages of the simulation—and al-

lowed γ to be deduced reliably within a few hundred time steps. This approach can be classified as a correlated sampling technique, which is more commonly employed in Monte Carlo than in molecular dynamics simulations, and was potentially first formulated in the context of nuclear physics [19].

For the computation of elastic constants, we impose a minuscule constant strain rather than a slowly ramped field, as in the original work. This simplifies the procedure, since it avoids the complications of maintaining constant stress. Two simulations are performed from the same equilibrated configuration and using identical random number sequences in the thermostat. The strain difference between the simulations is essentially free of thermal fluctuations—at least during the initial stages; however, care must be taken to suppress the effects of decorrelation at longer times.

The remainder of this paper is organized as follows: Section II introduces the fundamental concepts underlying the pursued method, while the relevant material-specific details are given in Section III. Section IV presents the results. Conclusions are drawn in Section V.

II. THEORY OF NOISE CANCELLATION

A. Preliminary considerations

Before elaborating on the ideas behind noise cancellation, it is worth substantiating our claim from the introduction that a 1% strain can change the elastic constants by more than 10%. As a simple illustration, we consider the Lennard–Jones (LJ) potential in its $m - n$ form [20], ($m = 12$, $n = 6$),

$$U(r) = U_0 \left[\left(\frac{r_0}{r} \right)^{12} - 2 \left(\frac{r_0}{r} \right)^6 \right], \quad (1)$$

where r is the distance between two atoms, U_0 the potential depth, and r_0 the equilibrium distance. The corresponding bond stiffness is

$$k_{12,6}(r) = \frac{12U_0}{r_0^2} \left[13 \left(\frac{r_0}{r} \right)^{14} - 7 \left(\frac{r_0}{r} \right)^8 \right]. \quad (2)$$

Using standard relations to connect such bond stiffnesses to elastic–tensor elements in simple solid structures [20], one finds that the ratio $k_{12,6}(0.99r_0)/k_{12,6}(r_0) \approx 1.23$ corresponds to roughly a 20% increase in the bulk modulus B .

For covalently bonded systems, the stiffening effect of the same compressive strain (1%) is smaller. For example, for the regular 2–1 (nearest–neighbor) Morse potential,

$$k_{2,1}(r) = \frac{2U_0}{r_0^2} \left[3 \left(\frac{r_0}{r} \right)^4 - \left(\frac{r_0}{r} \right)^3 \right], \quad (3)$$

one obtains $k_{2,1}(0.99r_0)/k_{2,1}(r_0) \approx 1.046$. Even so, an error approaching 5% can still be considered unsatisfactory.

The preliminary considerations discussed above highlight why computing the elastic constants of (amorphous) polymers presents particular challenges. Specifically, the steepness of the Lennard–Jones (LJ)–like interactions necessitates the use of very small strain increments in finite–difference (FD)–based schemes for reliable response–to–deformation (RTD) calculations. At the same time, the relatively low energy scales—characterized by small interaction prefactors (e.g., U_0 typically being below the thermal energy at room temperature)—make the system highly susceptible to thermal fluctuations. These combined effects contribute to significant noise in stress responses and complicate the accurate determination of the elastic tensor components.

B. Noise cancellation in ideally harmonic systems

To discuss the generic features of noise cancellation in harmonic and, to some degree, near–harmonic (extended) systems, we focus on a single but periodically repeated diatomic molecule in a simulation box. This molecule has a rigid, short bond (s) and a soft, long bond (l), both of which are approximated as harmonic, which captures the essential features of a linear, harmonic solid undergoing non–affine deformation under strain. The setup can be seen as a minimalist description of a zero–wavenumber optical vibration in an extended one–dimensional linear chain of H_2 molecules. A more realistic example would be the optical Γ –point vibration parallel to the direction of the Peierls distortion undergone by antimony from a simple cubic reference along [111].

The goal of the treatment presented hereafter is to understand how the mean stress and its standard deviation depend on time (shortly) after applying strain to an equilibrated sample. This proves useful to rationalize results and to identify first guidelines for convenient thermostat and parameter choices. For example, it will become clear why global kinetic energy controls (e.g., canonical sampling by velocity rescaling or Noé–Hoover) might not benefit from noise cancellation as much as stochastic thermostats do.

Following the discussion in the preceding paragraph, we introduce a minimal Hamiltonian for the enthalpy per unit cell,

$$H = \frac{k_s}{2} (hx_{21} - a_s^0)^2 + \frac{k_l}{2} \{h(1 - x_{21}) - a_l^0\}^2 - h\sigma, \quad (4)$$

where $k_s > k_l$ and $a_s^0 < a_l^0$ are the stiffnesses and equilibrium bond lengths of the short (s) and long (l) bonds, respectively. The box length per unit cell is denoted by h , in analogy to the h –matrix of constant–stress simulations [21], and $x_{21} = x_2 - x_1$. Here, x_i are reduced coordinates, with real positions $X_i = hx_i$. They do not appear in the final expressions but are required for intermediate steps. Reduced coordinates are also the natural variables in the constant–stress ensemble, ensuring a direct link between the analytical treatment and simulations.

Finally, σ is the external (tensile) stress. For readability, the kinetic-energy contribution is omitted here but will be included where necessary.

Minimizing H with respect to h , while keeping x_i (rather than a_s) constant, yields (the virial estimator for) the stress:

$$\sigma = -\frac{1}{h} \sum_{b=s,l} F_b a_b, \quad (5)$$

the generalization of which to higher dimensions is commonly used to deduce stress–tensor elements in molecular simulations. At a given value of h , a short–bond length of

$$a_s^{\text{eq}}(h) = \frac{k_s}{K} a_s^0 + \frac{k_l}{K} (h - a_l^0) \quad (6)$$

minimizes the energy, where $K = k_s + k_l$. Thus, the initial excess length of a short bond after an affine deformation is proportional to the applied strain ε , specifically

$$\Delta a_s^{\text{eq}}(t = 0^+) \equiv (1 + \varepsilon) a_s^{\text{eq}}(h) - a_s^{\text{eq}}\{(1 + \varepsilon)h\} \quad (7a)$$

$$= \frac{1}{K} \underbrace{(k_s a_s^0 - k_l a_l^0)}_{a'_s} \varepsilon, \quad (7b)$$

where the proportionality factor a'_s is commonly positive, since bond–length ratios are of order unity, while the stiffnesses of short (e.g., covalent) and long (e.g., dispersive) bonds tend to differ substantially.

Here, and in the following, Δ refers to a difference between an observable in the strained and reference (unstrained or oppositely strained) sample, e.g., $\Delta f \equiv f(0 < \varepsilon \ll 1) - f(0)$ denotes the difference between an observable at small finite strain and at zero strain. The quantity f is generally time dependent and can also be a compound property, such as products of forces and bond-lengths, Fa , to be considered further below. An exception to this rule is the time step Δt .

Assume now that a *thermal* solid, or an ensemble of equilibrated solids, is strained in an affine fashion from a reference shape h^{ref} to $h^{\text{str}} = (1 + \varepsilon)h^{\text{ref}}$ at the time $t = 0$. Both the strained solid (str) and the unstrained reference (ref) will then be propagated in time using the same random process, e.g., one based on Brownian or Langevin dynamics. To facilitate the treatment of the ensuing dynamics, we exploit the fact that our one–dimensional, two–body problem decomposes into the force–free center–of–mass motion and one internal eigenmode $a(t)$, e.g., $a_s(t)$, although $a_l(t)$ would have been an equally valid choice. The internal eigenmode(s) then obey(s) an equation of motion having the form of a harmonic oscillator with damping and noise,

$$\mu \delta \ddot{a}(t) + \frac{\mu}{\tau} \delta \dot{a}(t) + K \delta a(t) = \Gamma(t), \quad (8)$$

where $\delta a = a_s - a_s^{\text{eq}}\{(1 + \varepsilon)h\}$. Although it is the analogues of the x_n that are propagated in time by

the MD code, we can deduce the resulting dynamics by scrutinizing Eq. (8). In our specific example, μ is the reduced mass. The friction coefficient, μ/τ , defines a the damping time scale, τ . The thermal force $\Gamma(t)$ must have a vanishing first moment and otherwise obey $\langle \Gamma(t)\Gamma(t') \rangle = 2\mu k_B T \delta(t - t')/\tau$ to satisfy the fluctuation–dissipation theorem.

Just before the strain is applied, i.e., at time $t = 0^-$, the bond variable $a_s(t)$ can be decomposed into the equilibrium value, $\langle a_s(t = 0^-) \rangle = a_s^{\text{eq}}(h^{\text{ref}})$, and a thermal fluctuation $a_s(t = 0^-) - a_s^{\text{eq}}(h^{\text{ref}}) = \delta a^{\text{ref-}}$. Once the strain is applied, the bond variable is given by,

$$a_s^{\text{str}}(t = 0^+) = (1 + \varepsilon) \{a_s^{\text{eq}}(h^{\text{ref}}) + \delta a^{\text{ref-}}\} \quad (9a)$$

$$= a_s^{\text{eq}}(h^{\text{str}}) + \delta a^{\text{str+}}. \quad (9b)$$

This defines the new, initial bond excess $\delta a^{\text{str+}} = (1 + \varepsilon)\delta a^{\text{ref-}} + (1 + \varepsilon)a_s^{\text{eq}}(h^{\text{ref}}) - a_s^{\text{eq}}(h^{\text{str}})$.

At times $t > 0$, the formal solution of Eq. (8) reads

$$\delta a_s^{\text{str}}(t) = \delta a^{\text{str+}} C(t) + \underbrace{\int_0^t dt' G(t - t') \Gamma(t')}_{\equiv g(t)}, \quad (10)$$

where $C(t)$ and $G(t - t')$ are the relaxation and the Green’s function of the damped harmonic oscillator, respectively. Note that the thermostat–noise term, $g(t)$, is independent of the starting condition. Thus,

$$\Delta a_{\text{MD}}(t) = a^{\text{eq}}(h^{\text{str}}) - a^{\text{eq}}(h^{\text{ref}}) + \{\delta a^{\text{str+}} - \delta a^{\text{ref-}}\} C(t). \quad (11)$$

This is a deterministic function, except for the thermal noise present at $t = 0^-$, which vanishes on average. Thus, the bond length difference becomes a noise–free observable in the long run (i.e., for $t \gg \tau$) but only if $C(t)$ decays to zero. This is typically not the case in the microcanonical ensemble, corresponding to vanishing friction, $\tau \rightarrow \infty$, in Eq. (8), or, when using a thermostat based on global kinetic energy control, reinforcing arguments that such schemes do not always function as thermostats.

The absence of “new” ($t > 0$) random noise in $\Delta a_{\text{MD}}(t)$ might suggest a lack of noise in the stress estimator. However, this is not the case. The virial stress estimator depends on products of bond lengths and bond forces, both of which evolve dynamically over time. Consequently, fluctuations persist in the stress estimator, despite the apparent absence of new stochastic contributions in $\Delta a_{\text{MD}}(t)$. Furthermore, the two summands in Eq. (10) contribute in distinct ways, depending on whether the system is thermostatted or evolves in the same or similar way as in the microcanonical ensemble. Therefore, the variances associated with these contributions must be analyzed separately. In what follows, we focus on the thermostatted case.

Assuming a proper thermostat is present [22], the function $C(t)$ will decay over time, and asymptotically, only the term involving the Green’s function on the right–hand side of Eq. (10) will remain. We refer to this remaining noise term as $g(t)$. Once $C(t)$ in Eq. (10) has

effectively decayed to zero, $t \gg \tau$, a contribution to the virial estimator can be expressed as,

$$F_s a_s = K [a_s^{\text{eq}}(h) + g(t) - a_s^0] [a_s^{\text{eq}}(h) + g(t)]. \quad (12)$$

To facilitate the treatment, we restrict the remaining discussion to a stress-free reference, in which case $a_s^{\text{eq}}(h^{\text{ref}}) = a_s^0$ and $a_s^{\text{eq}}(h^{\text{str}}) = (1 + \varepsilon)a_s^{\text{eq}}(h^{\text{ref}}) + \varepsilon a'_s = a_s^0 + \varepsilon a'_0$, with a'_s from Eq. (7b). It follows that

$$F_s a_s = K [\varepsilon a'_0 + g(t)] [a_s^0 + \varepsilon a'_0 + g(t)] + \mathcal{O}(\varepsilon^2) \quad (13)$$

so that the difference expression with an unstrained reference becomes

$$\Delta(F_s a_s) = 2a'_0 \varepsilon [a_s^0 + g(t)] + \mathcal{O}(\varepsilon^2), \quad (14)$$

where a'_0 denotes the change of equilibrium bond length with ε relative to the (un-stressed) reference. Eq. (14) shows that the leading-order ratio of noise $g(t)$ to signal $a'_0 \varepsilon$ is independent of ε .

When the difference between the virial in the strained sample and the (exact) expectation value of the virial is taken in Eq. (14), an additional term proportional $g^2(t) - \langle g^2 \rangle$ arises, which does not vanish as ε tends to zero. This term causes poor signal-to-noise ratio when noise cancellation is not used.

To substantiate our calculations made in this section, Figure 1 compares the time-dependent estimate for the modulus of linear, ideally harmonic chains. To this end, a heterogeneous and a homogeneous chain are considered. The heterogeneous chain has short bonds ($a_s = 0.9$, $k_s = 10$) and long bonds ($a_l = 1.1$, $k_l = 0.52631\dots$), where the exact numerical value for k_l is chosen such that the static elastic modulus is $E_\infty = 1$. For the homogeneous chain, $a_s = a_l = 1$ and $k_s = k_l = 1$, also yielding $E_\infty = 1$. The heterogeneous chain is simulated at finite temperature ($T = 0.5$) and at zero temperature, while the homogeneous chain is only investigated at $T = 0.5$.

For the zero-temperature heterogeneous chain, the elastic modulus estimate quickly reaches its asymptotic value because the non-affine deformation, namely the stiff optical Γ -point mode, relaxes rapidly. In contrast, the finite-temperature homogeneous chain takes much longer to equilibrate, despite the absence of non-affine (athermal) deformations. This is because of low-frequency, long-wavelength modes. In fact, a single (overdamped) mode, i.e., the one at the Brillouin-zone boundary, dominates the elastic-constant estimator at large times, as can be seen from the single exponential indicated by the corresponding full line in Figure 1. The finite-temperature, heterogeneous chain displays both a fast initial relaxation due to the non-affine deformation and a slow final relaxation caused by the equilibration of long-wavelength acoustic modes. Note that the latter would add to the relaxation function $C(t)$, but are absent in the 2-body system.

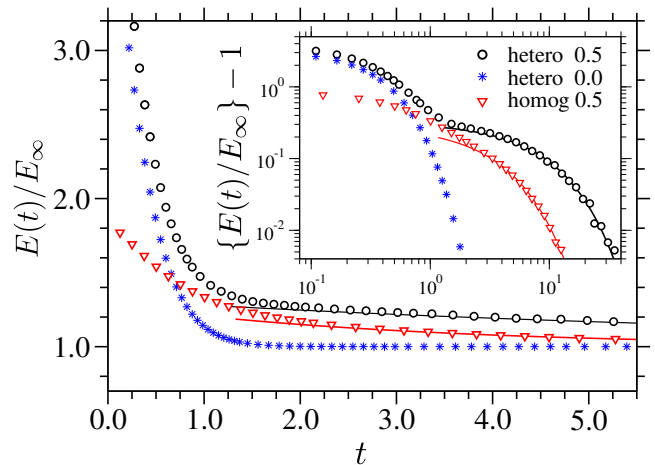


FIG. 1: Relaxation of the modulus $E(t)$ in a linear, ideally harmonic chain composed of three diatomic molecules. Three cases are shown: a heterogeneous (hetero) chain with alternating stiff, short bonds and soft, long bonds at finite temperature (black circles) and at zero temperature (blue stars), and a homogeneous (homog) chain with only one bond type. In all cases, the static modulus is $E_\infty = 1$. The inset displays the relative error of the estimate. Solid lines indicate fits using a single-exponential relaxation model, $E(t) = E_\infty + \Delta E \exp(-t/\tau)$.

C. Noise cancellation in quasi-harmonic systems

Interactions in real systems are never purely harmonic. Even simple model potentials, such as the Lennard-Jones potential, contain anharmonic contributions. Assuming a solid is nevertheless close to being harmonic, the potential energy can be approximated as

$$V(\varepsilon, \{u\}) \approx V_0(\varepsilon) + \sum_n \frac{k_{e,n}(\varepsilon)}{2} u_{e,n}^2, \quad (15)$$

where the anharmonicity is represented by the dependence of the Taylor coefficients on strain. The index e means to imply *eigen* so that $k_{e,n}$ is the stiffness associated with the n -th eigenmode $u_{e,n}$. In this quasi-harmonic approximation, the energy is truncated after the harmonic term, though it might be pragmatic to use effective values for $V_0(\varepsilon)$, which is the coefficient of interest, and $k_{e,n}$, e.g., to reproduce correctly the speed of sound in the continuum limit, rather than the “lateral” expansion coefficients.

In the realm of the noise-cancellation technique, we are primarily interested in deducing a difference of virial, which is dominated by the term $\Delta V = V_0(\varepsilon) - V_0(0)$ in a quasi-harmonic system. The difficulty that now arises in the quasi-harmonic approximation is that the harmonic contribution to the energy (difference) and thus the quasi-harmonic contribution to the stress and elastic-tensor estimators decorrelate over time, since the eigenstiffnesses, and thereby the eigenfrequencies $\omega_{e,n}$, depend on the strain. In lowest order, $\omega_{e,n}(\varepsilon) = \omega_{e,n}(0) + \omega'_{e,n} \varepsilon$.

Ignoring the effects of (implicit or explicit) damping, the difference between the *harmonic* potential energy terms caused by a (random) momentum transfer Δp at time Δt after impact will be

$$\Delta V_2 = \frac{\Delta p^2}{2m_e} [\sin^2\{\omega_e(\varepsilon)\Delta t\} - \sin^2\{\omega_e(0)\Delta t\}] \quad (16)$$

$$= \frac{\Delta p^2}{2m_e} \varepsilon \omega'_e \Delta t \sin\{2\omega_e(0)\Delta t\} + \mathcal{O}(\varepsilon^2). \quad (17)$$

Eq. (16) indicates that the stress estimators, which are proportional to $\Delta V_2/\varepsilon$, begin to deviate at a rate independent of ε . Initially, the deviation between the potential energy in the strained and reference samples grows as Δt^2 , as long as Δt remains small compared to the relevant phonon periods. Once Δt exceeds $1/\omega_e(0)$ but is still smaller than $1/\varepsilon\omega'_e$, the deviation grows linearly in time. However, a linear regime should not be expected in extended systems due to the broad distribution of eigenfrequencies. Because the (instantaneous) stress, and hence the elastic-constant estimator, scale with $\Delta V_2/\varepsilon$, the time dependence of the spurious contribution is, to leading order, independent of ε . This contribution is disadvantageous because it masks the genuine relaxation signal of self-affine modes.

In the limit of very large times, i.e., when $\varepsilon\omega'_e\Delta t \gg 1$, the two sinusoidal terms on the r.h.s. of Eq. (16) can be viewed as two independent random numbers with identical mean and each having a standard deviation (std) of $1/2$. Thus, the std of the *instantaneous* stress estimator will diverge as $1/\varepsilon$. This, however, does not imply that time averages suffer from the same problem. In fact, the “strained signal” is a delayed ($\omega'_e < 0$) or advanced ($\omega'_e > 0$) version of the reference signal, which leads to a systematic cancellation of integrated oscillations or fluctuations. The smaller ε , the more closely in time the strained and reference signals coincide. As a consequence, the std of an integrated signal decreases inversely with the observation time, $1/t_{\text{obs}}$. If the strained signal were obtained from a completely independent run, this scaling would be limited by what might be conveniently called the curse of stochastic sampling, i.e., reducing the error by a factor of two requires quadrupling the number of samples.

So far, we have discussed how strained and unstrained modes decorrelate in the absence of damping. This discussion thus pertains to the case when the damping is very small. In the opposite limit of large damping, the response to an instantaneous (thermal) force is suppressed before the modes decorrelate. This will lead to a finite, instantaneous std of the difference in the harmonic energy in the strained and the reference sample. This std will then remain independent of ε , even at large t . Thus, large damping is preferred to tame stochastic errors at large times, which, however, causes the deterministic relaxation to be slow.

Arbitrary damping can be dealt with in a straightforward fashion by using the exact Green’s function and

thermal random forces, i.e., second moments of the exact ΔV_2 by solving the Langevin equation, squaring the results, and finally summing over eigenmodes and taking expectation values. Instead of executing the just mentioned procedure, we find it more instructive to rationalize the behavior of a linear chain made, in which adjacent atoms interact through a Lennard–Jones potential. Such an analysis also contains non-linear terms and coupling between modes.

To this end, we consider a one-dimensional diatomic Lennard–Jones (LJ) chain consisting of three dimers with nearest-neighbor interactions. As in previous cases in Section II B, the LJ length scales for the short and long bonds are chosen as $r_{0,s} = 0.9$ and $r_{0,l} = 1.1$, respectively. The LJ energy parameter U_0 is selected to satisfy the stiffness criterion: $k_{1d} = 72U_0/r_0^2$. This expression corresponds to the curvature of the 6–12 LJ potential at its minimum, located at $2^{1/6}r_0$. The value of k_{1d} is chosen such that the zero-temperature, zero-stress reference state of the LJ chain matches the harmonic reference system previously analyzed in Section II B, i.e., the one defined by $k_s = 10$ and $k_l = 0.52631\dots$

To introduce large thermal fluctuations, we increase the temperature to $T = 0.5$. In this case, the atoms then go deeply into their repulsive interaction, leading to a modulus much in excess of the harmonic modulus where we increase the lattice constant of the reference system to $a_s + a_l = 3/2$, at which point E is still greater than unity. This choice might be seen as *ad-hoc*, in particular as one-dimensional systems with short-range interactions can be seen as artefactual, e.g., they lack phase transformations. However, sampling is extremely efficient and using the above choices for the one-dimensional LJ chain reproduces the trends of the full three-dimensional systems quite well. In this sense, the analysis of the one-dimensional LJ chain is meant to be a stepping stone between quasi-harmonic theory for a single Brillouin zone boundary vibration and a full three-dimensional system.

Figure 2 confirms similar trends for the one-dimensional LJ chain as those just discussed in Section II B. In particular, weaker damping leads to a faster relaxation of the expectation value for the elastic-constant estimator than large damping but also to more quickly growing variances.

The results for the linear LJ chain suggest that choosing thermostat time constants is not entirely straightforward. While it is tempting to formulate general guidelines, our attempts proved of limited value for the complex systems analyzed in the results section. In practice, trial and error was the most effective way to balance the slow initial relaxation caused by large damping against the large stochastic errors that arise at large simulation times with small damping.

While Figure 2 already confirmed the expectation that larger damping implies smaller standard deviation of the instantaneous measurements, Figure 3 corroborates this result using a double-logarithmic representation of the standard deviation as a function of time. This analysis

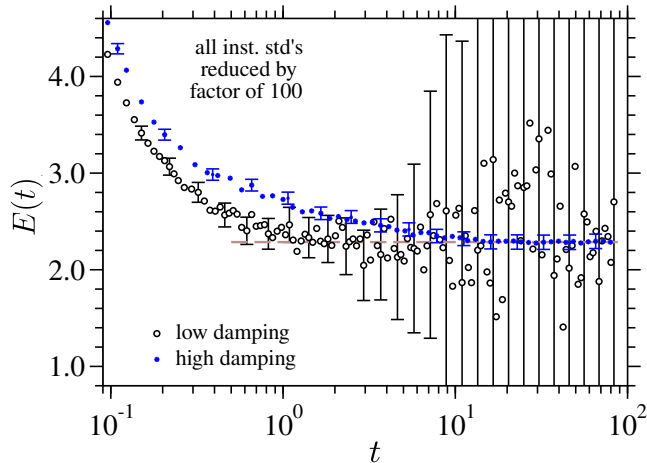


FIG. 2: Relaxation of the elastic-tensor estimator for a linear Lennard-Jones chain using the noise-cancellation technique with $\varepsilon = 10^{-3}$, shown for two relaxation times: $\tau = 0.109$ (large damping) and $\tau = 0.436$ (small damping). Averages were taken over 200,000 samples. Instantaneous error bars (std) have been reduced by a factor of 100 for clarity.

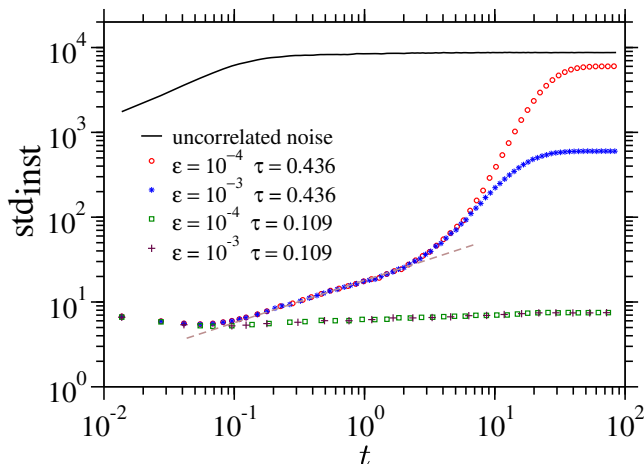


FIG. 3: Instantaneous standard deviation for data like that shown in Figure 2. In the calculation using uncorrelated random numbers for the follow-up runs, a strain of $\varepsilon = 10^{-4}$ was imposed and large damping $\tau = 0.109$ was used. The dashed line shows a \sqrt{t} power law.

also shows that the moment in time, when the standard deviation starts to increase does not depend on the strain ε , at least as long as it is sufficiently small. Moreover, after transiting through another regime, the std levels off at a larger final value as the strain decreases. Despite being large, the std remains far below the stochastic errors that one would obtain if the two follow-up simulations were run using a different set of random numbers. Perhaps, most importantly, when using sufficiently large damping, the long-time standard deviation is independent in leading order on ε .

Higher-order terms in the potential energy are not expected to change the results qualitatively if treatable by

perturbation theory. Any resulting corrections to the estimators scale with ε or higher, leaving the leading-order behavior intact.

Fig. 3 reveals that standard deviations can be large with non-optimized parameter choices. We thus explored the performance compared to the ‘traditional’ method using the Born term and a stress-fluctuation correction [5] for the linear LJ chain. We found a wide spread of results, with standard deviations ranging from being on par to being reduced by a factor of 100 when using the noise cancellation technique. However, while Born terms are readily evaluated for pair potentials, this is not true for many other potentials. Thus, the important message of Fig. 3 is that the noise cancellation technique yields smaller stochastic errors than uncorrelated differences.

III. MATERIALS, MODELS, AND NUMERICAL METHODS

We have tested the proposed method across a range of realistic models with increasing degrees of structural complexities, beginning with face-centered cubic argon, followed by crystalline silicon in the diamond structure and amorphous silicon, and concluding with amorphous polymers, specifically poly(methyl methacrylate) (PMMA), cellulose, and cellulose acetate. Schematic representations of the monomer structures of these polymers are shown in Figure 4. The simulations for argon and silicon were performed using the LAMMPS package [23], while polymer simulations were carried out using GROMACS [24].

A. Argon

In the argon simulations, individual particles interact via the standard 6–12 Lennard-Jones (LJ) potential, with an interaction energy of 0.2381 kcal/mol (10.32 meV) and a characteristic LJ length scale of 3.405 Å [25]. A cut-off distance of 9.0 Å is applied to truncate the interactions. The initial atomic configuration is generated as a face-centered cubic (FCC) lattice consisting of 500 atoms, using a lattice constant of $a = 5.311$ Å at $T = 10$ K [26]. The elastic tensor components C_{ij} are computed at a temperature of $T = 10$ K over a total simulation time of 10 ps, using a time step of $\Delta t = 1$ fs. Temperature control is achieved using a Langevin thermostat with Grønbech-Jensen algorithm [27], with a relaxation time constant of $\tau_T = 0.1$ ps. We note that the Debye temperature of crystalline argon is approximately 82 K; thus, the simulations are carried out well within the regime where the harmonic approximation remains valid in a classical treatment. For comparison, additional simulations were performed using the canonical sampling through velocity rescaling (CSVR) thermostat [28] and the microcanonical ensemble.

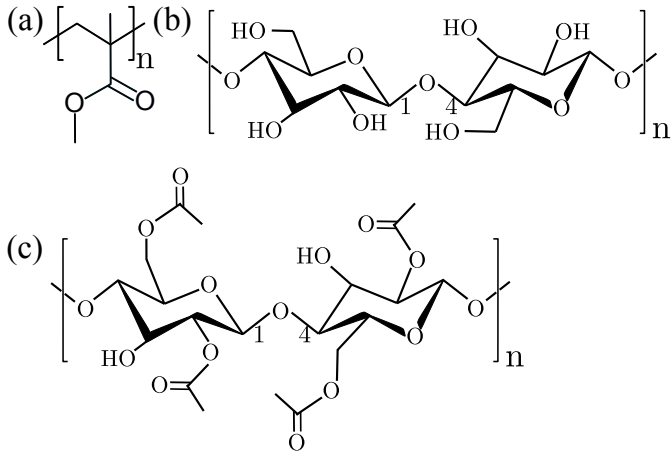


FIG. 4: Monomer structures of poly(methyl methacrylate) (part a), cellulose (part b), and cellulose acetate (part c) investigated in this study.

B. Silicon

Silicon simulations are conducted in two stages: (i) crystalline and (ii) amorphous configurations. In both cases, the systems consist of 1,000 silicon atoms. Atomic interactions are modeled using the modified Tersoff potential [29, 30].

The crystalline sample is initialized in the diamond cubic structure, using a lattice constant of $a = 5.431 \text{ \AA}$ [10]. Starting from this configuration, the amorphous melt is generated by heating the system to $T = 4,000 \text{ K}$ to induce melting. The resulting melt is then quenched to 300 K at a cooling rate of 1.48 K/ps using $\Delta t = 5 \text{ fs}$ and $\gamma_T = 1.0 \text{ ps}$. During this stage, a constant pressure of $p = 1 \text{ bar}$ is maintained using the Parrinello–Rahman barostat. The elastic tensor components C_{ij} are computed at $T = 300 \text{ K}$, with temperature controlled via a Langevin thermostat with Grønbech–Jensen algorithm [27], using a time constant $\tau_T = 0.01 \text{ ps}$. These simulations are typically run for 10 ps with a time step of $\Delta t = 1 \text{ fs}$. In some cases, the convergence of C_{ij} is also tested with different τ_T ; such details are reported where relevant. We have also tested alternative quenching protocols for preparing the amorphous silicon glass. The corresponding details are provided in Supplementary Section S1 [31].

C. Poly(methyl methacrylate)

As a representative example of an amorphous commodity polymer, we simulated a sample of poly(methyl methacrylate) (PMMA). The PMMA is modeled using modified OPLS–AA parameters [32], which have previously been shown to accurately capture the conformational behavior of single PMMA chains in solutions [32], as well as the heat capacity [33] and thermal conductivity [34] of solvent-free bulk PMMA. For this study, we employed a pre-equilibrated PMMA melt sample gen-

erated in earlier work [33]. The system comprises 100 PMMA chains, each with a degree of polymerization of $N_\ell = 30$. This leads to 45200 atoms in a PMMA sample.

The sample was equilibrated in the melt state at $T = 600 \text{ K}$ for at least $2 \mu\text{s}$, followed by quenching to $T = 300 \text{ K}$ [34], at which point the elastic tensor components C_{ij} were computed. Temperature control was achieved using a Langevin thermostat, and the simulations were carried out for 200 ps with a time step of $\Delta t = 0.4 \text{ ps}$. The thermostat coupling time was set to $\tau_T = 0.1 \text{ ps}$ for the production runs. Additionally, various damping schemes were implemented for the PMMA sample studied in this work; specific details are provided where relevant.

Long-range electrostatic interactions are handled using the particle–mesh Ewald (PME) method [35], and non-bonded interactions are truncated at a cutoff distance of $r_c = 1.0 \text{ nm}$.

D. Cellulose and cellulose acetate

We used pre-equilibrated amorphous samples of cellulose and cellulose acetate, previously generated in our recent study [36]. Both systems consist of 601 chains, each with a degree of polymerization $N_\ell = 50$. Cellulose and cellulose acetate samples consist of about 0.63 and 0.93 million atoms, respectively. To obtain well-equilibrated amorphous structures, the cellulose melt was equilibrated for $4.5 \mu\text{s}$ and cellulose acetate for $2.5 \mu\text{s}$ at $T = 800 \text{ K}$. After equilibration, both systems were gradually cooled to $T = 300 \text{ K}$, at which point the elastic tensor components C_{ij} were computed.

Cellulose was modeled using the GLYCAM06 force field [37, 38], which reliably captures the chair conformation of D-glucose rings forming the cellulose backbone. Simulations of the cellulose systems followed the same protocol as used for PMMA.

E. Computation of elastic tensor elements

In this work, we focus on the tetragonal shear modulus

$$G = \frac{C_{11} - C_{22}}{2}. \quad (18)$$

The reason for this choice is that shear moduli are smaller than bulk moduli and thus generally suffer from poorer signal to noise ratios, which puts large demands on our method. Moreover, the original motivation for this work stems from one of the authors' (DM) interest in computing high-precision shear modulus data for amorphous polymers using GROMACS [36]. Given that the cellulose samples contain approximately 0.63–0.93 million all-atom particles – and considering the known limitations of fluctuation-based methods – we compute the tetragonal shear modulus indirectly by applying a volume-

conserving strain to the system via;

$$\varepsilon_1 = \varepsilon \quad (19a)$$

$$\varepsilon_2 = \frac{1}{1 + \varepsilon} - 1 \quad (19b)$$

$$\varepsilon_{i \geq 3} = 0. \quad (19c)$$

In isotropic materials, this tetragonal shear modulus is equivalent to the conventional shear modulus. Approximating $\varepsilon_2 \approx 1 - \varepsilon$ for the small ε values, we thus find for systems of cubic or higher symmetry

$$\sigma_{1,2} = \pm(C_{11} - C_{12})\varepsilon \quad (20)$$

so that G can be deduced in leading order via

$$G = \frac{\sigma_1 - \sigma_2}{2\varepsilon}. \quad (21)$$

Other elements of the elastic tensor could be deduced through related box-deformations, e.g., C_{11} by leaving all strain-tensor elements zero, except for ε_1 . In this case, noise cancellation might best be done by deducing C_{11} from taking the difference signal of two strained simulations via

$$\begin{aligned} C_{11} &= \frac{\sigma_1(\varepsilon_i = \varepsilon\delta_{i,1}) - \sigma_1(\varepsilon_i = -\varepsilon\delta_{i,1})}{2\varepsilon} \\ C_{12} &= \frac{\sigma_2(\varepsilon_i = \varepsilon\delta_{i,1}) - \sigma_2(\varepsilon_i = -\varepsilon\delta_{i,1})}{2\varepsilon} \end{aligned} \quad (22)$$

Ultimately, by choosing various “shapes” for the strain tensor, all C_{ij} can be determined. By considering different magnitudes in the strains, the systematic expansion of the (free) energy beyond quadratic terms can be targeted.

IV. RESULTS

To further detail the method and to substantiate claims made in Section II, the time evolution of elastic modulus estimators in Eq. (21) and Eq. (22) will be scrutinized for selected samples using selected approaches.

A. Effect of thermostat

The calculation in Section II B was based on the assumption that $C(t)$ in Eq. (10) has decayed. Thermostatting should therefore aim to achieve this decay as efficiently as possible. Therefore, we begin by examining the impact of thermostat choice on simulations of crystalline argon and silicon, as shown in Figure 5 and Figure 6. Interestingly, the widely used canonical sampling through velocity rescaling (CSVr) thermostat [28]—a global kinetic energy control method—produces dynamics that closely resemble those of the microcanonical (NVE) ensemble. While all schemes appear to level off at a similar estimate for the shear modulus at very

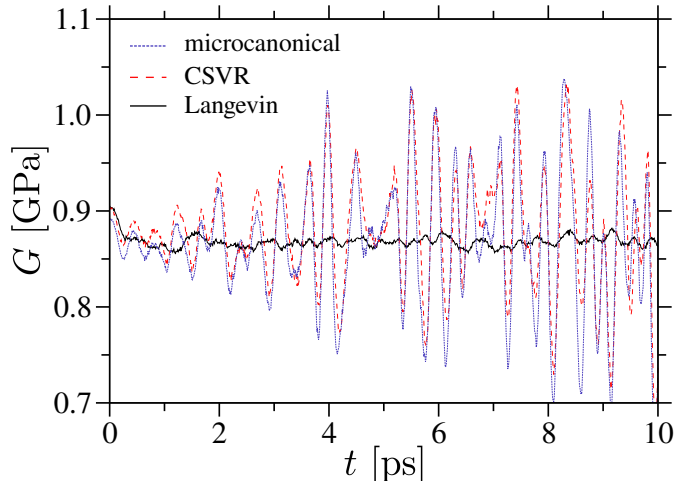


FIG. 5: Time evolution of the tetragonal shear modulus estimator defined in Equation (21) for crystalline argon at a temperature $T = 10$ K. Different integration schemes are used: microcanonical (blue, dotted line), canonical sampling by velocity rescaling (CSVr, red, dashed lines), and Langevin (full, black line) using the Grønbech–Jensen algorithm.

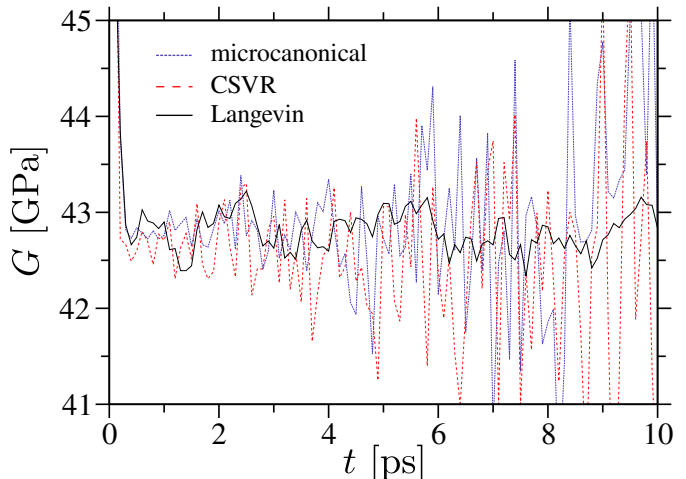


FIG. 6: Same as Figure 5, however, for silicon at a temperature $T = 300$ K.

early times, a notable difference, however, emerges in the later relaxation between thermostatted dynamics (solid black line) and pseudo-microcanonical schemes (dotted blue and dashed red lines). This difference arises because the microcanonical ensemble does not enable energy exchange between vibrational modes, which can limit convergence of the shear modulus, G , over time—particularly in nearly harmonic systems. Increasing the system size reduces the stochastic noise. Additional simulations on crystalline silicon, in which the system size was increased from $N = 1,000$ to $8,000$, suggest that this reduction obeys the usual curse of stochastic sampling, i.e., that system sizes have to be quadrupled to double the signal-to-noise ratio (data not shown).

Despite above discrepancies— between the properly thermostatted and microcanonical simulations— in transient behavior, the time-averaged values of G differ by less than 1.5% across the different approaches. However, the associated statistical uncertainty— estimated via block-averaged standard deviations— exceeds 10% for both the NVE and CSVN ensembles, while it drops to approximately 0.5% when using the Langevin thermostat [27]. Although similar trends are observed for both crystalline argon at $T = 10$ K and silicon at $T = 300$ K (both well within their respective harmonic limits, i.e., significantly below the Debye temperature), the case of silicon is more nuanced due to non-affine displacements of the basis atoms in the diamond structure under anisotropic deformation. Note that the quantum fluctuations only alter elastic constants well below the Debye temperature [12, 39, 40].

We note in passing why the microcanonical setup exhibits large fluctuations. Ideally, in the absence of external noise, it should yield a well-converged value. However, as shown in Eq. (10), the Green’s function term, $g(t)$, vanishes, leaving only the first term, which barely decays over time without explicit damping.

In addition to the system-size dependence of the signal-to-noise ratio, one may be concerned about finite-size effects in the signal itself. For crystalline systems, this is typically minor, as sufficiently large simulation cells effectively provide a “ k -point sampling” in the sense of the trapezoidal rule and the response is dominated by the $k = 0$ contribution. In macroscopically homogeneous but microscopically disordered systems, more pronounced finite-size effects must be expected. In practice, corrections will become small once the linear simulation cell size exceeds at least twice the structural (Ornstein–Zernike) correlation length (typically around 1.5 nm), and, in the case of polymers, the corresponding end-to-end distance. With linear box sizes of 7.8 nm for PMMA [33], 18.0 nm for cellulose, and 21.6 nm for cellulose acetate [36], our simulations satisfy these criteria comfortably so that finite-size effects are expected to remain small.

B. Effect of thermostat damping time

In Figures 2 and 3, we demonstrated the influence of damping on the elastic modulus estimator for a one-dimensional Lennard–Jones chain. As discussed, the relaxation function $C(t)$ in Eq. (10) decays most rapidly when a mode is critically damped. In real systems, however, the presence of a distribution of eigenfrequencies complicates this behavior. For practical equilibration, it is crucial to efficiently relax those modes that contribute most significantly to the decay of the initial excess stress. Since non-affine deformations are typically localized— at least in homogeneous materials— the relevant vibrational modes tend to lie at higher frequencies. Therefore, it is advantageous to first target the high-frequency vibra-

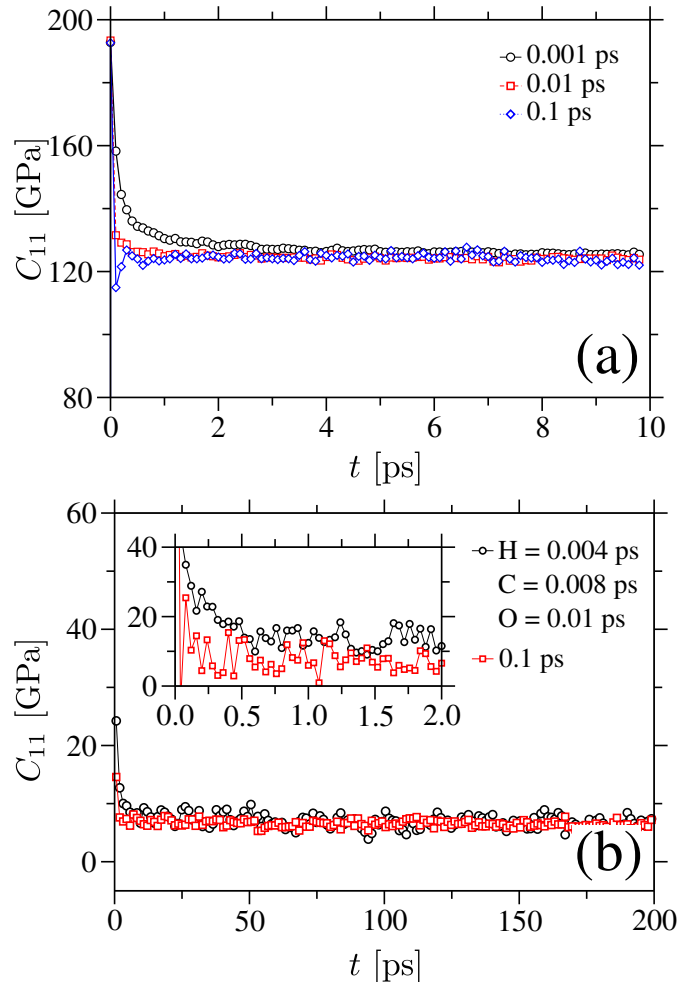


FIG. 7: The temporal relaxation of the elastic modulus C_{11} is shown for two amorphous systems: amorphous silicon (panel a) and poly(methyl methacrylate) (PMMA) (panel b). The inset in panel (b) highlights the short-time relaxation behavior ($t \leq 2$ ps) of C_{11} . Each panel displays data corresponding to different damping times of the Langevin thermostat. For clarity, the data in the main panel (b) have been coarse-grained, averaging every 32 data points into one.

tional modes associated with stiff bonds, such as OH, CH, and CC bonds in polymers [33].

Since the stress in stiff covalent bonds is the dominant contribution to the excess stress after an affine deformation, it is meaningful to first use a relatively short thermostat time constant, such that the fastest modes become critically damped. During this initial stage, most of the excess stress is rapidly reduced. However, other non-affine modes, such as those related to torsional motion, will be overdamped and thus hindered in their relaxation. For this reason, it can be beneficial to follow the initial run, or, rather pairs of runs, with one or more subsequent runs using a substantially longer thermostat time constant. The need for such runs and the optimal choice of parameters will generally depend on the specific system under study. If this second phase is omitted, slow

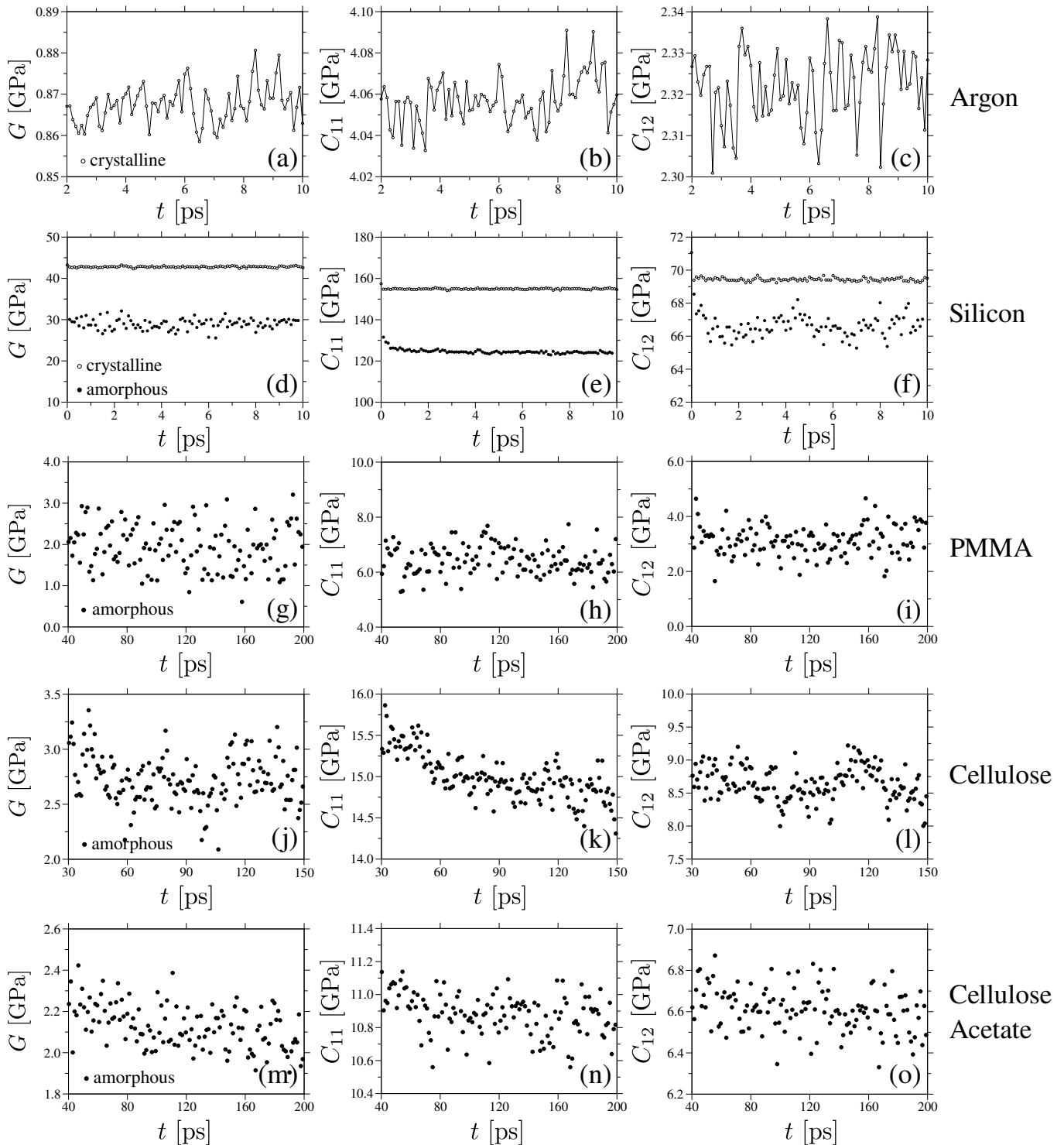


FIG. 8: Notably, the results for crystalline argon and silicon are averaged over 1 and 16 independent runs, respectively, while the amorphous silicon data represent an average over 49 runs. For all polymer systems, the reported values are averaged over 100 independent simulations. The polymer data shown herein have been coarse-grained for clarity.

relaxation of the signal can persist, potentially leading to incorrect conclusions about the flow behavior of the system studied.

Using accurate integration schemes, such as the one

proposed by Grønbech-Jensen [27], one can choose relatively large time steps such that the fastest quasi-harmonic mode can be relaxed within roughly few hundred MD steps— though running a few more does no

harm. If the second stage targets modes with periods ten times longer than the fastest ones, approximately ten times more time steps will be needed, since the fastest modes still limit the timestep size. In principle, the procedure can be iterated, and the scaling of the thermostat time constant can be optimized. However, it may also be advantageous to conduct the follow-up simulation with the lowest-frequency mode critically damped. Ideally, the simulation should then run long enough for a transverse sound wave to traverse the simulation cell.

Further optimizations may be needed, especially since small damping produces large instantaneous (though not necessarily time-averaged) asymptotic standard deviations. In principle, one would expect it to be beneficial if the broad spectrum of frequencies in non-elemental systems were somewhat collapsed if atoms participating particularly strongly in high-frequency vibrations were made heavier. However, in the relevant cases investigated for polymers, the benefits appeared to be limited. Instead it proved more useful to use shorter damping time constants for the light hydrogen atoms than for the heavier carbon atoms. The reason could be that torsional and other slow modes were less overdamped by this procedure.

Another optimization is to not apply an ideally affine strain. For example, only the center of mass and/or the backbone of a polymer could be subjected to an affine transformation, while the remaining internal degrees of the polymers remain unaltered. In this case, ligands and side groups could be re-attached to the backbone atom using unaltered distance vectors.

C. Applications

Figure 7 presents results for two different samples, each simulated using a range of Langevin damping times τ_T . At small damping times—where stiff vibrational modes are critically damped—they equilibrate rapidly. However, this also leads to a slower overall relaxation of C_{11} . In contrast, larger damping times result in slower equilibration of high-frequency modes, but the average value around which they fluctuate converges more quickly to the long-time relaxed value of C_{11} . A trend that is also evident for the simplified model in Figure 2.

We note in passing that the silicon system exhibits a relatively narrow range of characteristic vibrational frequencies, where we have attempted one damping time. However, for polymers—such as PMMA—which possess a broad spectrum of eigenfrequencies [33], we have also used various Langevin damping schemes with a goal to explore different possibilities to improve the data. These details are highlighted in the Supplementary Section S1.

In Figure 7(b), the PMMA data correspond specifically to damping schemes (i) and (ii) discussed in the Supplementary Section S1 for the elastic modulus C_{11} . A full set of PMMA results for all elastic constants obtained using these damping strategies is provided in the

Supplementary Figure S2 [31].

For the production runs of all systems studied in this work, we selected damping times, τ_T , that ensure rapid convergence of the elastic constants, C_{ij} , to their reference values. Added advantage of the single damping time scheme is that it is easy to implement even in the complex polymeric systems. Figure 8 summarizes the time evolution and convergence behavior of C_{ij} for each system. Notably, after the initial rapid relaxation, the amorphous samples exhibit a secondary, slower decay in the elastic constants C_{ij} over time. This effect becomes increasingly pronounced with greater structural complexity—for instance, the decay is noticeably slower in amorphous cellulose compared to amorphous silicon (see Figures 8e, k, and n). A similar two-stage relaxation trend is observed in the case of the generic diatomic harmonic chain with thermal fluctuations (see Figure 1). At first glance, and in the absence of the theoretical insights provided by Figure 1, this transient behavior might be misinterpreted as an indication of flow or irreversible deformation within the sample. To rule out this possibility, we conducted a series of additional simulations involving energy minimization on pre-strained cellulose samples. In these tests, the atomic coordinates remained unchanged after relaxation to the next energy minimum between the initial and final configurations (data not shown), thereby confirming the absence of any flow-like behavior. Taken together, these observations suggest that the slow decay in C_{ij} is not due to structural rearrangements but rather arises from intrinsic vibrational eigenfrequencies of the system. Specifically, the broad distribution of eigenfrequencies characteristic of polymeric and amorphous materials leads to a slow convergence of the elastic response. In particular, the overpopulation of low-frequency vibrational modes—commonly referred to as the Boson peak [41, 42]—is a key factor underlying the long-time decay of C_{ij} .

A summary of the averaged C_{ij} values, along with available literature data for comparison, is provided in Supplementary Table I. Overall, the results exhibit good agreement with previously published values, thereby supporting the consistency and reliability of our computational approach. In the case of silicon, our estimates align much better with previous simulations [46] than with experimental results [47], where discrepancies are particularly large for the shear modulus of the amorphous solid. We believe that this is mostly caused by deficiencies of the potential rather than by our comparatively large quench rates, which produce less stable structures than slower cooling protocols. We come to this conclusion, because changing the quench rate by an order of magnitude barely changes G , as shown in the Supplementary Section S1 and Supplementary Figs. S1 and S2. Moreover, estimates of C_{11} are already off by 10 GPa for the crystal, which has a well-defined reference structure. Thus, force-field induced errors of order 10 GPa in all elastic tensor elements must be expected. However, what matters most for our work, in which we aim

TABLE I: Average values of the elastic modulus components. They are computed by block-averaging over ten blocks taken from the second half of the data shown in Figure 8. The standard errors are calculated across these ten blocks. For comparison, available literature data for different systems are also included. In all quoted experimental values, G was obtained from $G = (C_{11} - C_{12})/2$.

Crystalline samples				
System	Source	G [GPa]	C_{11} [GPa]	C_{12} [GPa]
Argon	This work	0.868 ± 0.001	4.069 ± 0.002	2.325 ± 0.001
	Previous sim. [12]	–	3.9	–
	Experiment [43]	1.0	4.0	2.0
Silicon	This work	42.80 ± 0.03	154.93 ± 0.04	69.42 ± 0.02
	Experiment [44]	51	166	64
	Experiment [45]	52.2	171.5	67.1
Amorphous samples				
System	Source	G [GPa]	C_{11} [GPa]	C_{12} [GPa]
Silicon	This work	28.1 ± 0.2	124.1 ± 0.1	66.5 ± 0.1
	Previous sim. [46]	25.2	131.0	81.4
	Experiment [47]	48.8	156	58.4
PMMA	This work	1.85 ± 0.07	6.37 ± 0.06	3.15 ± 0.07
	Experiment [48]	2.0 ± 0.1	9.6 ± 0.9	–
Cellulose	This work	2.71 ± 0.03	14.84 ± 0.02	8.62 ± 0.03
Cellulose Acetate	This work	2.09 ± 0.01	10.85 ± 0.02	6.59 ± 0.01

to establish a lean method for the computation of elastic constants, is that previous simulations [46] using similar potentials find similar values as we do. Analyzing the shortcoming of the potential for a covalently bonded solid and suggesting how to mitigate deficiencies is beyond the scope of this work. Since non-covalent interaction, which primarily dictate the elastic tensor coefficients in polymeric systems, have a much reduced many-body character compared to interactions in covalently bonded solids, we expect our results on polymers to better compare to real systems than for silicon.

Notably, the values reported for cellulose and cellulose acetate are predictive in nature, as– to the best of our knowledge– no corresponding C_{ij} data are currently available in the simulation or experimental literature. These predictions provide a valuable reference point for future studies. Furthermore, the computed C_{ij} values for cellulose derivatives across a range of temperatures have already been successfully employed to estimate thermal transport coefficients κ in related work [36], which was the main motivation behind the development of the noise-cancellation approach proposed herein. Lastly, we emphasize that kinetic-energy contribution to the computed C_{ij} values are negligible in all cases, remaining below 0.1%, and therefore do not influence the reported results.

The optimal approach will certainly be system-specific. Metamaterials with extended domains of soft and stiff regions, which may allow liquid intrusions,

are likely to require longer simulations for each thermostat time constant, particular care when applying the strain, and additional measures to make the noise-cancellation technique sufficiently efficient for meaningful results. Discussing such complex systems in detail is beyond the scope of this work. Nevertheless, it is clear that achieving the optimum balance between fast relaxation of the first moment of stress estimators and keeping stochastic errors small will be extremely challenging, since the first goal benefits from small damping while the second benefits from large damping.

V. CONCLUSIONS

In this work, we have developed and applied a practical and generalizable method for accurately computing elastic constants at finite temperature, addressing common challenges associated with thermal noise and anharmonicity in molecular simulations. By extending a noise-cancellation approach previously applied to piezoelectric coefficients [18], we have introduced a protocol that relies on computing stress differences between strained and unstrained (or oppositely strained) configurations, all evolved under identical thermostating conditions. This setup effectively cancels out the dominant contributions of thermal fluctuations, allowing for low-variance estimates of elastic constants. Importantly, our

findings highlight a key advantage of this approach: it does not rely on fitting stress–strain curves or on time-averaged fluctuations of stress or strain, both of which are commonly hampered by noise and slow convergence at finite temperature. This is particularly relevant for modern materials science, where increasingly complex materials – ranging from amorphous semiconductors to bio-derived polymers – require reliable mechanical characterization at the nanoscale, i.e., over volumes large enough to define local elastic properties yet small enough to capture heterogeneity in structure.

We validated the method across a diverse set of material systems, beginning with crystalline argon as a simple benchmark and progressing through ordered and amorphous silicon to structurally complex amorphous polymers such as poly(methyl methacrylate) and cellulose derivatives. In each case, our results show rapid and stable convergence of the elastic constants, with reasonable agreement with available reference data. For the polymeric systems, especially cellulose and cellulose acetate, our simulations provide the first calculation of the full elastic tensor at finite temperature, offering valuable new data for the materials modeling community. We have further applied this method to determine the temperature-dependent elastic constants of a cellulose derivative and their direct implications for thermal transport [36], as well as the elastic constants of experimentally relevant commodity polymers under high pressures [49] and poly-electrolyte melts [50]. While the current work utilizes a simple forward-difference scheme to demonstrate the robust performance of the noise cancellation technique even under non-ideal conditions, moving to a central-difference scheme would offer an immediate path to further increasing numerical stability. Such an approach would likely simplify the optimization of strain magnitudes by extending the range over which anharmonic effects remain negligible.

The method proposed in this work targets exclusively the (quasi-)static elastic constants. The noise-cancellation technique still bears the possibility to deduce viscoelastic response functions. To this end, a pair of constant-stress simulations would have to be per-

formed, one under zero stress and another one under a constant perturbative stress. The (expectation value of the) difference in the strain between these two runs, divided by the stress increment, allows the time-dependent and thus frequency-dependent elastic modulus to be deduced. The signal-to-noise ratio in this approach will certainly be much improved compared to a direct measurement without noise cancellation. Nonetheless, decorrelation of the signal, which is expected to set in once the long-wavelength modes start relaxing, may require special measures to ensure meaningful results at medium and large time scales.

Beyond its immediate application to elasticity, the methodology introduced here has potential extensions to other finite-temperature response properties, particularly the specific heat, whose calculation relies on differences analogous to those used for elastic constants. Furthermore, its simplicity and compatibility with standard molecular dynamics frameworks make it easily adaptable to a wide range of computational workflows. We expect this approach to enable more accurate mechanical modeling across disciplines — including condensed matter physics, polymer science, and biomaterials engineering — and to provide a foundation for future developments in finite-temperature materials simulations.

Acknowledgment: D.M. thanks Tiago Espinosa de Oliveira for a collaboration [36], which provided key systems investigated in this work. Financial support for D.M. and M.M. was provided by the Bundesministerium für Technologie, Forschung und Raumfahrt (BMTRF) within the project 16ME0658K MExMeMo and European Union–NextGenerationEU. The authors gratefully acknowledge the Gauss Centre for Supercomputing e.V. (www.gauss-centre.eu) for providing computing time through the John von Neumann Institute for Computing (NIC) on the GCS Supercomputer JUWELS at Jülich Supercomputing Centre (JSC) where the polymer simulations were performed. M.H.M. acknowledges helpful discussions with Sergey Suhomlinov and Lars Pastewka.

-
- [1] M. Born and K. Huang, *Dynamical Theory of Crystal Lattices*. Oxford, UK: Oxford University Press, 1954.
- [2] M. Parrinello and A. Rahman, “Strain fluctuations and elastic constants,” *The Journal of Chemical Physics*, vol. 76, no. 5, pp. 2662–2666, 1982.
- [3] J. R. Ray and A. Rahman, “Statistical ensembles and molecular dynamics studies of anisotropic solids,” *The Journal of Chemical Physics*, vol. 80, no. 9, p. 4423–4428, 1984.
- [4] D. Squire, A. Holt, and W. Hoover, “Isothermal elastic constants for argon. theory and monte carlo calculations,” *Physica*, vol. 42, p. 388–397, May 1969.
- [5] J. F. Lutsko, “Generalized expressions for the calculation of elastic constants by computer simulation,” *Journal of Applied Physics*, vol. 65, p. 2991–2997, Apr. 1989.
- [6] K. Huang, “On the atomic theory of elasticity,” *Proc. R. Soc. London, Ser. A*, vol. 203, no. 1073, pp. 178–194, 1950.
- [7] T. H. K. Barron and M. L. Klein, “Second-order elastic constants of a solid under stress,” *Proc. Phys. Soc.*, vol. 85, no. 3, pp. 523–532, 1965.
- [8] W. Shinoda, M. Shiga, and M. Mikami, “Rapid estimation of elastic constants by molecular dynamics simulation under constant stress,” *Phys. Rev. B*, vol. 69, p. 134103, Apr 2004.
- [9] E. B. Tadmor and R. E. Miller, *Modeling Materials:*

- Continuum, Atomistic and Multiscale Techniques*. Cambridge University Press, 2011. Available online: <https://doi.org/10.1017/CB09781139003582>.
- [10] J. Griebner, L. Frérot, J. A. Oldenstaedt, M. H. Müser, and L. Pastewka, “Analytic elastic coefficients in molecular calculations: Finite strain, nonaffine displacements, and many-body interatomic potentials,” *Phys. Rev. Mater.*, vol. 7, p. 073603, 2023.
- [11] J. R. Ray, “Elastic constants and statistical ensembles in molecular dynamics,” *Computer Physics Reports*, vol. 8, p. 109–151, Aug. 1988.
- [12] P. Schöffel and M. H. Müser, “Elastic constants of quantum solids by path integral simulations,” *Phys. Rev. B*, vol. 63, p. 224108, 2001.
- [13] D. A. Folkner, Z. Chen, G. Barbalinardo, F. Knoop, and D. Donadio, “Elastic moduli and thermal conductivity of quantum materials at finite temperature,” *Journal of Applied Physics*, vol. 136, Dec. 2024.
- [14] C. E. Maloney and A. Lemaître, “Amorphous systems in athermal, quasistatic shear,” *Physical Review E*, vol. 74, July 2006.
- [15] M. Tsamados, A. Tanguy, C. Goldenberg, and J.-L. Barrat, “Local elasticity map and plasticity in a model lennard-jones glass,” *Physical Review E*, vol. 80, Aug. 2009.
- [16] V. Vaibhav, T. W. Sirk, and A. Zacccone, “Time-scale bridging in atomistic simulations of epoxy polymer mechanics using nonaffine deformation theory,” *Macromolecules*, vol. 57, no. 23, pp. 10885–10893, 2024.
- [17] J. Griebner and L. Pastewka, “Vibrational lifetimes and viscoelastic properties of ultrastable glasses,” *Physical Review E*, vol. 110, Aug. 2024.
- [18] D. Herzbach and M. H. Müser, “Piezoelectric coefficients by molecular dynamics simulations in the constant stress ensemble: A case study of quartz,” *Computer Physics Communications*, vol. 174, no. 1, pp. 17–23, 2006.
- [19] H. Rief, “Generalized monte carlo perturbation algorithms for correlated sampling and a second-order taylor series approach,” *Annals of Nuclear Energy*, vol. 11, p. 455–476, Jan. 1984.
- [20] M. H. Müser, S. V. Sukhomlinov, and L. Pastewka, “Interatomic potentials: achievements and challenges,” *Advances in Physics: X*, vol. 8, Nov. 2022.
- [21] M. Parrinello and A. Rahman, “Polymorphic transitions in single crystals: A new molecular dynamics method,” *J. Appl. Phys.*, vol. 52, no. 12, p. 7182, 1981.
- [22] S. Agarwal, S. V. Sukhomlinov, M. Honecker, and M. H. Müser, “Advanced langevin thermostats: Properties, extensions to rheology, and a lean momentum-conserving approach,” *The Journal of Chemical Physics*, vol. 163, p. 124110, 09 2025.
- [23] A. P. Thompson, H. M. Aktulga, R. Berger, D. S. Bolintineanu, W. M. Brown, P. S. Crozier, P. J. in’t Veld, A. Kohlmeyer, S. G. Moore, T. D. Nguyen, et al., “Lammps—a flexible simulation tool for particle-based materials modeling at the atomic, meso, and continuum scales,” *Computer Physics Communications*, vol. 271, p. 108171, 2022.
- [24] M. J. Abraham, T. Murtola, R. Schulz, S. Páll, J. C. Smith, B. Hess, and E. Lindahl, “Gromacs: High performance molecular simulations through multi-level parallelism from laptops to supercomputers,” *SoftwareX*, vol. 1., pp. 19–25, 2015.
- [25] A. Rahman, “Correlations in the motion of atoms in liquid argon,” *Phys. Rev.*, vol. 136, pp. A405–A411, 1964.
- [26] C. S. Barrett and L. Meyer, “X-ray diffraction study of solid argon,” *The Journal of Chemical Physics*, vol. 41, no. 4, pp. 1078–1081, 1964.
- [27] N. Grønbech-Jensen and O. Farago, “A simple and effective verlet-type algorithm for simulating langevin dynamics,” *Molecular Physics*, vol. 111, no. 8, pp. 983–991, 2013.
- [28] G. Bussi, D. Donadio, and M. Parrinello, “Canonical sampling through velocity rescaling,” *Journal of Chemical Physics*, vol. 126, p. 014101, 2007.
- [29] J. Tersoff, “New empirical approach for the structure and energy of covalent systems,” *Phys. Rev. B*, vol. 37, pp. 6991–7000, 1988.
- [30] T. Kumagai, S. Izumi, S. Hara, and S. Sakai, “Development of bond-order potentials that can reproduce the elastic constants and melting point of silicon for classical molecular dynamics simulation,” *Computational Materials Science*, vol. 39, no. 2, pp. 457–464, 2007.
- [31] “Electronic supplementary information—document number to be added by the editors,”
- [32] D. Mukherji, C. M. Marques, T. Stühn, and K. Kremer, “Depleted depletion drives polymer swelling in poor solvent mixtures,” *Nature Communications*, vol. 8, p. 1374, 2017.
- [33] H. Gao, T. P. W. Menzel, M. H. Müser, and D. Mukherji, “Comparing simulated specific heat of liquid polymers and oligomers to experiments,” *Phys. Rev. Mater.*, vol. 5, p. 065605, 2021.
- [34] D. Mukherji, “Computing the thermal transport coefficient of neutral amorphous polymers using exact vibrational density of states: Comparison with experiments,” *Physical Review Materials*, vol. 8, p. 085601, 2024.
- [35] T. Darden, D. York, and L. Pedersen, “Particle mesh ewald: An N-log(N) method for ewald sums in large systems,” *The Journal of Chemical Physics*, vol. 98, no. 12, pp. 10089–10092, 1993.
- [36] D. Mukherji, T. E. de Oliveira, N. Chowdhury, D. G. Cahill, and M. Müller, “Heat flow in solvent-free, dense amorphous and semi-crystalline cellulose derivatives,” *Macromolecules*, vol. 59, no. 0, p. 575, 2026.
- [37] K. N. Kirschner, A. B. Yongye, S. M. Tschampel, J. González-Outeiriño, C. R. Daniels, B. L. Foley, and R. J. Woods, “Glycam06: A generalizable biomolecular force field. carbohydrates,” *Journal of Computational Chemistry*, vol. 29, no. 4, pp. 622–655, 2008.
- [38] S.-J. Park, J. Lee, Y. Qi, N. R. Kern, H. S. Lee, S. Jo, I. Joung, K. Joo, J. Lee, and W. Im, “Charmm-gui glycan modeler for modeling and simulation of carbohydrates and glycoconjugates,” *Glycobiology*, vol. 29, no. 4, pp. 320–331, 2019.
- [39] R. Martoňák, W. Paul, and K. Binder, “Orthorhombic phase of crystalline polyethylene: A constant pressure path-integral monte carlo study,” *Phys. Rev. E*, vol. 57, pp. 2425–2437, Feb 1998.
- [40] M. H. Müser, “Simulation of material properties below the debye temperature: A path-integral molecular dynamics case study of quartz,” *The Journal of Chemical Physics*, vol. 114, pp. 6364–6370, 04 2001.
- [41] F. Leonforte, R. Boissière, A. Tanguy, J. P. Wittmer, and J.-L. Barrat, “Continuum limit of amorphous elastic bodies. iii. three-dimensional systems,” *Phys. Rev. B*, vol. 72, p. 224206, Dec 2005.
- [42] J. Horbach, W. Kob, and K. Binder, “The dynamics

- of supercooled silica: acoustic modes and boson peak,” Journal of Non-Crystalline Solids, vol. 235-237, pp. 320–324, 1998.
- [43] H. Meixner, P. Leiderer, P. Berberich, and E. Lüscher, “The elastic constants of solid argon determined by stimulated brillouin scattering,” Physics Letters A, vol. 40, no. 3, pp. 257–258, 1972.
- [44] J. J. Hall, “Electronic effects in the elastic constants of *n*-type silicon,” Phys. Rev., vol. 161, pp. 756–761, 1967.
- [45] J. D. Schall, G. Gao, and J. A. Harrison, “Elastic constants of silicon materials calculated as a function of temperature using a parametrization of the second-generation reactive empirical bond-order potential,” Phys. Rev. B, vol. 77, p. 115209, Mar 2008.
- [46] C. L. Allred, X. Yuan, M. Z. Bazant, and L. W. Hobbs, “Elastic constants of defected and amorphous silicon with the environment-dependent interatomic potential,” Phys. Rev. B, vol. 70, p. 134113, 2004.
- [47] G. De Sandre, L. Colombo, and C. Bottani, “Calculation of elastic constants in defected and amorphous silicon by quantum simulations,” Phys. Rev. B, vol. 54, pp. 11857–11860, Nov 1996.
- [48] X. Xie, D. Li, T. Tsai, J. Liu, P. V. Braun, and D. G. Cahill, “Thermal conductivity, heat capacity, and elastic constants of water-soluble polymers and polymer blends,” Macromolecules, vol. 49, pp. 972–978, 2016.
- [49] O. H. Moura de Alencar, J. Wu, M. Müller, and D. Mukherji, “Thermal conductivity of commodity polymers under high pressures,” The Journal of Chemical Physics, vol. 164, p. 024905, 01 2026.
- [50] D. Mukherji and M. Müller, “Linking electrostatic-induced chain stretching to heat flow in amorphous polymers,” 10.26434/chemrxiv.15000116, 2026.